J. Fluid Mech. (1996), *vol.* 325, *pp.* 53–77

Dynamic simulation of suspensions of non-Brownian hard spheres

By D. I. DRATLER† AND W. R. SCHOWALTER
Department of Chemical Engineering, University of Illinois, Urbana, IL 61801, USA

(Received 14 August 1995 and in revised form 21 May 1996)

In this work, we investigate the suitability of models based solely on continuum hydrodynamics for Stokesian Dynamics simulations of sheared suspensions of non-Brownian hard spheres. The suspensions of interest consist of monolayers of uniform rigid spheres subjected to a linear shear field. Areal fractions ranged from $\phi_a = 0.2$ to 0.6. For these suspensions, two sets of Stokesian Dynamics simulations were performed. For the first set, particle interactions were assumed to be strictly hydrodynamic in nature. These simulations are analogous to those of Brady & Bossis (1985) and Chang & Powell (1993). For the second set of simulations, particles were subjected to both hydrodynamic and short-range repulsive forces. The repulsion serves as a qualitative model of non-hydrodynamic effects important when particle separation distances are small. Results from both sets of simulations were found to be within the range of established experimental data for viscosities of suspensions. However, simulations employing the pure hydrodynamic model lead to very small separation distances between particles. These small separations give rise to particle overlaps that could not be eliminated by time-step refinement. The instantaneous number of overlaps increased with density and typically exceeded the number of particles at the highest densities considered. More critically, for very dense suspensions the simulations failed to approach a long-time asymptotic state. For simulations employing a short-range repulsive force, these problems were eliminated. The repulsion had the effect of preventing extremely small separations, thereby eliminating particle overlaps. At high concentrations, viscosities computed using the two methods are significantly different. This suggests that the dynamics of particles near contact have a significant impact on bulk properties. Furthermore, the results suggest that a critical aspect of the physics important at small particle separation distances is missing from the pure hydrodynamic model, making it unusable for computing microstructures of dense suspensions. In contrast, simulations employing a short-range repulsive force appear to produce more realistic microstructures, and can be performed even at very high densities.

1. Introduction

Dynamic simulation is a powerful tool for studying the microscopic and macroscopic behaviour of granular media such as suspensions, pure fluids, sand, etc. At the microscopic level, dynamic simulation entails application of Newton's second law of motion to the individual particles in the substance. From time integration of these equations, microscopic particle configurations, or the microstructure, are obtained. Macroscopic properties can then be computed from the known microstructure. For

† Present address: Exxon Production Research Company, P.O. Box 2189, Houston, TX 77252-2189, USA.

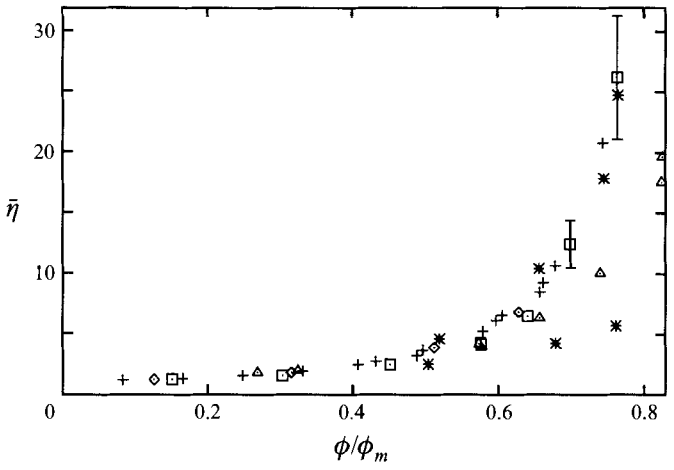

FIGURE 1. Comparison of relative viscosities $\bar{\eta}$ obtained from Stokesian Dynamics simulations to experimental data. Simulations of Brady & Bossis (1985) (◇) and Chang & Powell (1993) (⊡) are of monolayer suspensions of non-Brownian monodisperse hard spheres subject to a linear shear flow. Data of Chang & Powell (1993) are shown with errorbars if errorbars were used in their original presentation. Experimental data of Lewis & Nielsen (1968) (+) are for glass spheres of four different mean diameters: 7, 34, 51 and 95 μm. Experimental data of Sengen & Probstein (1989) (△) are for styrene spheres with diameters in the range 200–300 μm. Experimental data presented in Thomas (1965) (✱) are from a number of different published sources. A limited number of these data, illustrating the variability of measured viscosities of dense suspensions, are shown. For the simulations, $\phi = \phi_a$ and $\phi_m = \pi/4$. For the experimental data, $\phi = \phi_v$ and $\phi_m = \pi/(3\sqrt{3})$.

suspensions of colloidal particles, a dynamic simulation method known as Stokesian Dynamics has been developed (see Bossis & Brady 1984; Durlofsky, Brady & Bossis 1987; and Brady *et al.* 1988). Stokesian Dynamics can be used for applications in which particle motion is governed by hydrodynamic, interparticle, Brownian, and external forces. In addition, because multi-body hydrodynamic interactions and the effects of lubrication layers between nearly touching particles are included in its formulation, this method is not restricted to dilute systems. As a result, Stokesian Dynamics can be used for investigating phenomena important in very dense suspensions.

Stokesian Dynamics has seen extensive use in investigations of suspension rheology (see e.g. Brady & Bossis 1985, 1988; Bossis & Brady 1989; Durlofsky & Brady 1989; Bonnecaze & Brady 1992; Chang & Powell 1993; Phung & Brady 1991). Brady & Bossis (1985) and Chang & Powell (1993) employed Stokesian Dynamics to study the high-shear limiting rheology of suspensions of hard spheres, i.e. dispersions of rigid spheres in which the only forces governing particle motion are hydrodynamic in origin. Relative viscosities obtained by these investigators are shown in figure 1, where they are compared to the experimentally measured viscosities of Lewis & Nielsen (1968) and Sengen & Probstein (1989). In addition, a limited number of measured viscosities presented in Thomas (1965) are shown: these viscosities, which were obtained from a number of different published sources, exhibit a high degree of variability. Here we show a limited number of these data points to illustrate this variability. To facilitate comparison of the simulated viscosities, which are for monolayer suspensions, to the experimental data, the simulated and experimentally measured viscosities are plotted as functions of ϕ_a/ϕ_m and ϕ_v/ϕ_m respectively. Here ϕ_a is areal fraction, ϕ_v is volume fraction, and ϕ_m is taken as the maximum areal or volume fraction at which suspensions can flow homogeneously. Following Brady & Bossis (1985), we have set $\phi_m = \pi/4$ for the simulated viscosities and $\phi_m = \pi/(3\sqrt{3})$ for the experimental data.

The simulated viscosities are seen to agree quite well with the experimental data of Lewis & Nielsen (1968) for all densities shown. In contrast, for $\phi_a \gtrsim 0.50$ the simulated viscosities are significantly larger than the measured viscosities of Sengen & Probstein (1989). However, the Thomas (1965) data indicate a high degree of variability in measured viscosities at high densities. Therefore, given that both sets of simulation results, as well as the data of Lewis & Nielsen (1968) and Sengen & Probstein (1989), fall within the bounds suggested by the Thomas (1965) data, the comparison between the simulations and the experimental data seems reasonable.

Despite the reasonable viscosities obtained by Brady & Bossis (1985) and Chang & Powell (1993), there is a fundamental inconsistency with the use of Stokesian Dynamics to simulate suspensions of non-Brownian hard spheres that has not been addressed in the cited work. This inconsistency is the use of a pure hydrodynamic and continuum-mechanics-based model (i.e. Stokesian Dynamics) to simulate suspensions for which extremely small particle separations occur. Bossis & Brady (1984) noted that dimensionless surface-to-surface particle separations of $O(10^{-8})$ routinely occur in simulations of dense hard-sphere suspensions. For the $O(100\ \mu\text{m})$ particles used in the experiments of Lewis & Nielsen (1968) and Sengen & Probstein (1989), a dimensionless separation of 10^{-8} is equivalent to a dimensional separation of $O(10^{-12}\ \text{m})$. Non-hydrodynamic forces, surface roughness effects, and non-continuum phenomena are expected to be important at these small separations (Bossis & Brady 1984), but have not been incorporated in previous investigations that employed Stokesian Dynamics. Moreover, the consequences of omitting these phenomena have not been investigated to date.

From a computational standpoint, the presence of extremely small particle separations necessitates the use of a very small time step when calculating particle trajectories. In the absence of a sufficiently small time step, Bossis & Brady (1984) noted that numerical errors can cause particles to overlap. However, they also noted that overlaps could be eliminated, at great expense, by reducing the time step. Although particle overlaps are typically quite small, they are problematic since hydrodynamic forces associated with overlapping particles are undefined. To circumvent this problem, Bossis & Brady (1984) developed the following method to accommodate the presence of overlapping particles. When pairs of particles overlapped, hydrodynamic forces were computed as if the overlapping particles were actually separated by a small gap. As a result, particles could overlap without causing termination of the calculation. This technique was employed in the simulations of Brady & Bossis (1985) and Chang & Powell (1993). However, a detailed study of the influence of particle overlaps, which can be quite numerous at high densities, on computed suspension microstructures and bulk properties has not been performed.

In the current work, we present a detailed study of the problems that arise when using Stokesian Dynamics to simulate sheared suspensions of hydrodynamically interacting spherical particles, i.e. suspensions of non-Brownian hard spheres. The simulations discussed are analogous to those of Brady & Bossis (1985) and Chang & Powell (1993). As we will show, a number of problems arise with these types of simulations, particularly at high densities. In agreement with Bossis & Brady (1984), our results indicate the presence of very small particle separations in the computed microstructure that give rise to overlaps between adjacent particles. These overlaps could not be eliminated by reducing the time step. Furthermore, the number of particle overlaps tended to be large at high densities. For $\phi_a = 0.60$, we observed in excess of 40 overlaps in instantaneous configurations containing 25 particles. Clearly, one must be wary of results in which the number of overlaps far exceeds the number of particles.

These results merit reporting because they were obtained from simulations essentially identical to those discussed in Brady & Bossis (1985) and Chang & Powell (1993). An additional problem at high densities is that simulations do not approach an asymptotic state at long times, and therefore do not exhibit the behaviour expected of real suspensions. Instead, simulations terminate prematurely due to the presence of large overlaps between adjacent particles in the suspension. This anomalous behaviour could not be eliminated with time-step reductions. Based on the results reported here, we conclude that the purely hydrodynamic model is not satisfactory at high densities.

We also present results of Stokesian Dynamics simulations in which particles interact through hydrodynamic and short-range repulsive forces. This repulsion serves a number of purposes. First, the repulsion prevents the occurrence of extremely small particle separations, with the minimum particle separation in the suspension fixed by the range of the interparticle force. Secondly, although not based on a rigorous model of phenomena important at very small length scales, the repulsion can be thought of as a qualitative representation of forces, such as those due to molecular interactions, that might be important when particles are near contact. Finally, for all densities considered in this work, repulsion eliminated all particle overlaps.

We will show that simulations employing a short-range repulsive force have a number of desirable features not seen in simulations based on a purely hydrodynamic model of particle interactions. First, simulations reach an asymptotic state quite quickly, with bulk properties exhibiting well-defined long-time averages. In the absence of repulsion, long-time averages tend to vary to a much greater degree. In addition, computed microstructures appear to be more realistic and do not contain overlaps. As a result, simulations do not terminate due to excessive overlap as is observed in simulations based on a pure hydrodynamic model. Finally, computed viscosities are found to be in reasonable agreement with experimental data.

2. Simulation method

We consider a suspension of rigid spherical particles of uniform size dispersed in a Newtonian liquid. The suspension is assumed infinite in extent and subject to an imposed velocity field given by

$$\boldsymbol{u}^{\infty} = (\dot{\gamma} y, 0, 0), \tag{1}$$

where the vector $\boldsymbol{u}^{\infty}$ denotes the bulk velocity of the suspension, $\dot{\gamma}$ is the shear rate of the imposed flow, and y denotes distance in the shear gradient direction. To reduce the computational cost of the simulations, we follow Brady & Bossis (1985) and Chang & Powell (1993) and restrict particles to the (x, y)-plane, the plane of shear. The suspension geometry and the coordinate system are shown in figure 2. Particles in suspension are assumed sufficiently small that the particle Reynolds number may be taken as zero, and sufficiently large that Brownian motion may be neglected. Therefore, the motion of the suspended particles can be assumed to be governed by a balance of hydrodynamic and interparticle forces.

For the conditions described above, Stokesian Dynamics can be used to compute the transient behaviour of the suspension microstructure and the bulk viscosity. This method is outlined in detail in Brady *et al.* (1988). Here we simply give an overview of the method. To facilitate simulations of infinite monolayer suspensions, we consider a finite system of N particles that is periodically replicated throughout the (x,y)-plane. Prior to shearing, this N-particle system resides in a square computational domain of dimensions $h_{cell} \times h_{cell}$. Assuming a known configuration of particles, Durlofsky *et al.*

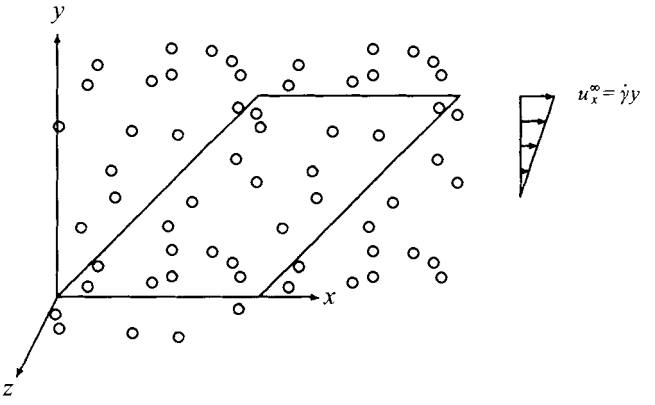

FIGURE 2. Schematic representation of computational domain, which contains N particles that all lie in the (x, y)-plane. Prior to shear the domain is square with dimensions $h_{cell} \times h_{cell}$. The suspension is subjected to an imposed shear flow given by $\boldsymbol{u}^\infty = (\dot{\gamma} y, 0, 0)$.

(1987) have shown that the translational and rotational velocities of the particles can be related to the hydrodynamic forces, torques, and stresslets exerted on the suspended particles through the relations

$$\begin{pmatrix} \boldsymbol{F}_h \\ \boldsymbol{S}_h \end{pmatrix} = \begin{pmatrix} \boldsymbol{R}_{FU} & \boldsymbol{R}_{FE} \\ \boldsymbol{R}_{SU} & \boldsymbol{R}_{SE} \end{pmatrix} \cdot \begin{pmatrix} \boldsymbol{U}^\infty - \boldsymbol{U} \\ \boldsymbol{E}^\infty \end{pmatrix}. \tag{2}$$

In (2), the vector $\boldsymbol{F}_h$ contains the forces and torques exerted on the N suspended particles by the fluid; $\boldsymbol{S}_h$ contains the three non-zero independent components of the hydrodynamic stresslet, S_{hxx}, S_{hyy}, and S_{hxy}, exerted on each of the N particles; $\boldsymbol{U}$ contains the translational and rotational velocities of the N suspended particles; $\boldsymbol{U}^\infty$ contains the translational and rotational components of the bulk velocity that would exist at the particle centres in the absence of the particles; and $\boldsymbol{E}^\infty$ contains the e_{xx}, e_{yy}, and e_{xy} components of the bulk rate-of-strain tensor that would exist at the particle centres in the absence of the particles. For the bulk velocity field described by (1), the rate-of-strain tensor is constant with components $e_{xx} = e_{yy} = 0$ and $e_{xy} = \frac{1}{2}$. The quantities $\boldsymbol{R}_{FU}$, $\boldsymbol{R}_{FE}$, $\boldsymbol{R}_{SU}$, and $\boldsymbol{R}_{SE}$ are configuration-dependent resistance tensors. For the monolayer suspensions of interest in this work, forces and translational velocities associated with each particle are restricted to the (x, y)-plane while torques and rotational velocities associated with each particle are restricted to the z-direction. As a result, the vectors in equation (2) have dimension $3N$ and the tensors have dimension $3N \times 3N$. In (2) and for the remainder of this paper, displacements are non-dimensionalized by the sphere radius a, translational velocities by $\dot{\gamma} a$, rotational velocities by $\dot{\gamma}$, time by $1/\dot{\gamma}$, viscosity by the solvent viscosity η_s, strain rates by $\dot{\gamma}$, forces by $6\pi\eta_s a^2\dot{\gamma}$, and torques and stresslets by $6\pi\eta_s a^3\dot{\gamma}$.

Equation (2) is derived from an integral solution of Stokes equations, written in a form that is convergent in the limit $N \to \infty$. Combining this integral solution with Faxén expressions for spherical particles and a multipole moment expansion (Durlofsky *et al.* 1987) leads to expressions relating the translational and rotational velocities of the N particles to moments of the hydrodynamic force density exerted on the N particles. These equations can be expressed in the form

$$\begin{pmatrix} \boldsymbol{U}^\infty - \boldsymbol{U} \\ \boldsymbol{E}^\infty \end{pmatrix} = \begin{pmatrix} \boldsymbol{M}_{UF} & \boldsymbol{M}_{US} \\ \boldsymbol{M}_{EF} & \boldsymbol{M}_{ES} \end{pmatrix} \cdot \begin{pmatrix} \boldsymbol{F}_h \\ \boldsymbol{S}_h \end{pmatrix}, \tag{3}$$

where $\boldsymbol{M}_{UF}$, $\boldsymbol{M}_{US}$, $\boldsymbol{M}_{EF}$, and $\boldsymbol{M}_{ES}$ are configuration-dependent mobility tensors. Equation (3) incorporates far-field hydrodynamic interactions between particles, including interactions involving particles that reside in image domains. These interactions can be efficiently incorporated into the mobility tensors using an Ewald sum. Using the Ewald sum, the strength of hydrodynamic interactions decays rapidly with increasing distance between the computational domain and image domains. Therefore, only image domains relatively close to the computational domain need be explicitly included in the formulation of (3). In this work, image domains are included if they abut the computational domain, or if they abut image domains that abut the computational domain. To maintain positive-definite mobility tensors, the monolayer must also be periodically replicated in the z-direction. These periodic images are located at $z = \pm z_{cell}$ and $z = \pm 2z_{cell}$, with $z_{cell} \gg h_{cell}$ to minimize the influence of these images on particles in the computational domain. The computational domain is located at $z = 0$. Tests were conducted to ensure that variations in z_{cell} and variations in the number of image domains employed in the formulation of (3) did not significantly influence simulation results. Equation (3) contains only far-field hydrodynamic interactions. To include near-field interactions, (3) is inverted to yield an expression of the form of (2). Near-field hydrodynamic interactions are then included in a pairwise additive manner.

Particle velocities are computed from a force and torque balance on the suspended particles. Applying Newton's second law to the particles, and neglecting inertia due to the small size of the particles, leads to

$$\boldsymbol{F}_h + \boldsymbol{F}_p = \boldsymbol{0}, \tag{4}$$

where $\boldsymbol{F}_h$ is as defined above and $\boldsymbol{F}_p$ is a vector of dimension $3N$ containing the two components of force and the one component of torque exerted on each of the suspended particles by interparticle forces. Because the particles are spherical, non-hydrodynamically induced torques, and therefore hydrodynamically induced torques, are identically zero. Combining equations (2) and (4) leads to

$$\boldsymbol{R}_{FU} \cdot (\boldsymbol{U} - \boldsymbol{U}^{\infty}) = \boldsymbol{F}_p + \boldsymbol{R}_{FE} : \boldsymbol{E}^{\infty}, \tag{5}$$

which is a $3N \times 3N$ system of linear algebraic equations. For a known configuration of particles, equation (5) can be solved for the unknown velocities $\boldsymbol{U}$. Therefore, given a known initial configuration of particles, the temporal variation of particle positions and velocities can be obtained through solution of (5) and numerical integration of $\boldsymbol{U}$. For this work, a fourth-order Adams–Bashforth scheme (Conte & de Boor 1980) is used for the numerical integration. Equation (5) is solved directly using a Cholesky decomposition. To reduce the computational costs associated with computing $\boldsymbol{R}_{FU}$ and $\boldsymbol{R}_{FE}$, the mobility tensors $\boldsymbol{M}_{UF}$, etc., which contain only far-field hydrodynamic interactions and therefore vary slowly with time, are recomputed at time intervals of T_{inv} instead of at every time step.

With the suspension microstructure and velocities known, the bulk stress or viscosity can be obtained. The bulk stress in a suspension is defined as the average stress in a volume that is both much larger than the characteristic particle spacing and much smaller than the macroscopic length scale of the suspension (Batchelor 1970). Employing this definition, one can write an expression for the suspension viscosity that takes the form

$$\eta = 1 + \underbrace{3\phi_a \frac{1}{N} \sum_{\alpha=1}^{N} \Theta_{xy}^{\alpha}}_{\eta_h} + \underbrace{3\phi_a \frac{1}{N} \sum_{\alpha=1}^{N} \Psi_{xy}^{\alpha} + 3\phi_a \frac{1}{N} \sum_{\alpha=1}^{N} \sum_{\beta=1}^{\alpha-1} F_{p,x}^{\alpha\beta} (y_\beta - y_\alpha)}_{\eta_p} \tag{6}$$

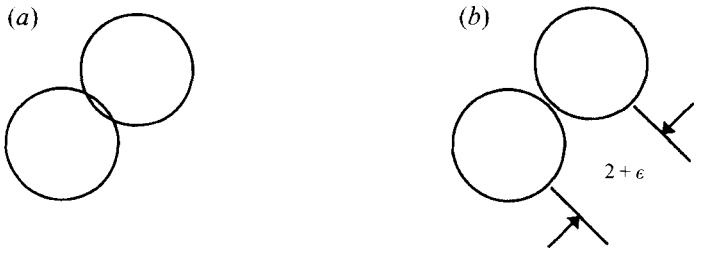

FIGURE 3. Schematic of particle configurations used to compute hydrodynamic forces associated with overlapping particles: (*a*) two overlapping particles, with the overlap magnified for clarity; (*b*) the configuration used to compute the hydrodynamic forces associated with the overlapped particles. The particles are not actually moved.

(see Bonnecaze & Brady 1992), where ϕ_a is the suspension areal fraction, $F^{\alpha\beta}_{p,x}$ is the x-component of the interparticle force exerted on particle α by particle β, $y_\beta - y_\alpha$ is the distance in the shear-gradient direction from the centre of particle α to the centre of particle β, and $\Theta^\alpha_{xy} + \Psi^\alpha_{xy} = S^\alpha_{hxy}$ where S^α_{hxy} is the (x, y)-component of the hydrodynamic stresslet exerted on particle α by the fluid. The quantity Θ^α_{xy} is the component of S^α_{hxy} that arises from the bulk motion while Ψ^α_{xy} is the component of S^α_{hxy} that arises from interparticle forces. In vector form, $\Theta + \Psi = \boldsymbol{S}_h$, with Θ and Ψ obtained from

$$\Theta = (\boldsymbol{R}_{SE} - \boldsymbol{R}_{SU}\boldsymbol{R}^{-1}_{FU}\boldsymbol{R}_{FE}) : \boldsymbol{E}^\infty \tag{7}$$

and

$$\Psi = -\boldsymbol{R}_{SU}\boldsymbol{R}^{-1}_{FU}\boldsymbol{F}_p. \tag{8}$$

In this work, the first sum in equation (6) will be referred to as the hydrodynamic viscosity η_h, while the combination of the second and third sums in (6) will be referred to as the viscosity due to interparticle forces η_p.

Time averages of η, denoted by $\bar{\eta}$, are computed in the time interval $T_e \leqslant t \leqslant T_s$, where T_s is the final time of the simulation and T_e is the equilibration time of η. In this work, we conservatively estimate the equilibration time to be the time at which the running average of η ceases to vary significantly. Statistical errors in $\bar{\eta}$ are determined using the sub-average method outlined in Allen & Tildesley (1987).

3. Simulation of suspensions of hard spheres

To simulate suspensions in which particles are subjected only to hydrodynamic forces, one can set $\boldsymbol{F}_p = \boldsymbol{0}$ and perform simulations as outlined in §2. However, in the absence of repulsive interparticle forces, particle separations can become quite small. Bossis & Brady (1984) noted that these small separations, in combination with numerical errors associated with the integration of U, can lead to overlapping particles. Although they found these overlaps to be quite small, they are problematic since lubrication forces between closely separated particles are singular at contact and undefined for the unphysical situation of overlapping particles. To avoid these problems, Bossis & Brady (1984) employed the following procedure for computing hydrodynamic forces associated with overlapping pairs of particles. For pairs of particles with centre-to-centre separations less than $2+\epsilon$, where $0 < \epsilon \ll 1$, which includes all overlapping pairs as well as pairs separated by a gap smaller than ϵ, the centre-to-centre separation was assumed to be $2+\epsilon$ for the purpose of computing hydrodynamic forces. However, the particles were not actually moved. With the above

procedure, the singularity associated with touching particles and the ambiguity associated with computing hydrodynamic forces for overlapping pairs of particles are avoided. A schematic representation of the two-particle configurations used in place of overlapping two-particle configurations is shown in figure 3.

As will be shown in §4, a number of problems arise when performing simulations using the above approach, including the occurrence of extremely small particle separations that invalidate the continuum hydrodynamic model used for the simulations, and the presence of large numbers of overlapping particles in computed configurations. Therefore, we have investigated an alternative approach in which extremely small particle separations and overlaps are prevented by allowing particles to be repulsive at very small separations. The repulsive force has the effect of setting a minimum spacing in the suspension, which can eliminate problems associated with extremely small particle separations. Similar methods have been used in Brownian Dynamics simulations of hard-sphere suspensions (Heyes & Melrose 1993). In our work, the repulsive force is taken as

$$\boldsymbol{F}_p^{\alpha\beta} = \frac{\tau}{\gamma^*} \frac{\mathrm{e}^{-\tau h}}{1+\mathrm{e}^{-\tau h}} \frac{\boldsymbol{r}_{sep}}{|\boldsymbol{r}_{sep}|}, \tag{9}$$

where $\boldsymbol{F}_p^{\alpha\beta}$ is the force on particle α exerted by particle β, $\boldsymbol{r}_{sep}$ is the centre-to-centre separation vector directed from particle β to particle α, τ controls the decay rate of $\boldsymbol{F}_p^{\alpha\beta}$, and $h = |\boldsymbol{r}_{sep}| - 2$. The parameter γ^* is equal to $(6\pi\eta_s a^2\dot{\gamma})/(2F_0)$, where τF_0 is the dimensional magnitude of $\boldsymbol{F}_p^{\alpha\beta}$ at contact. Equation (9) has the same form as the Derjaguin formula for the repulsive force between two like-charged spheres with constant surface potentials (Russel, Saville & Schowalter 1989). However, we have demonstrated in tests that the precise form of $\boldsymbol{F}_p^{\alpha\beta}$ is unimportant provided it decays rapidly to zero with increasing particle separation.

4. Results

In this section, results of Stokesian Dynamics simulations of suspensions of non-Brownian hard spheres are presented. For the results presented in §4.1, $\boldsymbol{F}_p = \boldsymbol{0}$ so particle overlaps do occur. Hydrodynamic forces associated with these overlapping particles are computed using the method outlined in Bossis & Brady (1984) (see §3). For the results presented in §4.2, particles are repulsive with $\boldsymbol{F}_p$ given by equation (9). For these simulations, particles never overlapped.

For the simulations presented, areal fractions ranged from $\phi_a = 0.20$ to 0.60. For most of the simulations $N = 25$, but a limited number was also performed with $N = 36$, 49 and 64. However, as results did not change significantly with N, results are presented for the $N = 25$ simulations only. We note that $N = 25$ is the number of particles employed in the simulations of Brady & Bossis (1985) and the $\phi_a = 0.60$ monodisperse simulations of Chang & Powell (1993). Initial configurations consisted of particles randomly positioned in the computational domain. Except as noted below, all simulations were run for 500 dimensionless time units ($T_s = 500$). However, as a precaution against reporting results for which the extent of overlap between adjacent particles is quite large, simulations were stopped whenever the amount of overlap between two particles exceeded 2% of a particle radius. Although arbitrary, 2% is in accord with the amount of overlap reported by Bossis & Brady (1984) for their simulations of moderately dense suspensions. Simulations for $\boldsymbol{F}_p = \boldsymbol{0}$ and $\phi_a = 0.60$ tended to terminate prior to $T_s = 500$ due to the presence of overlaps in excess of 2%.

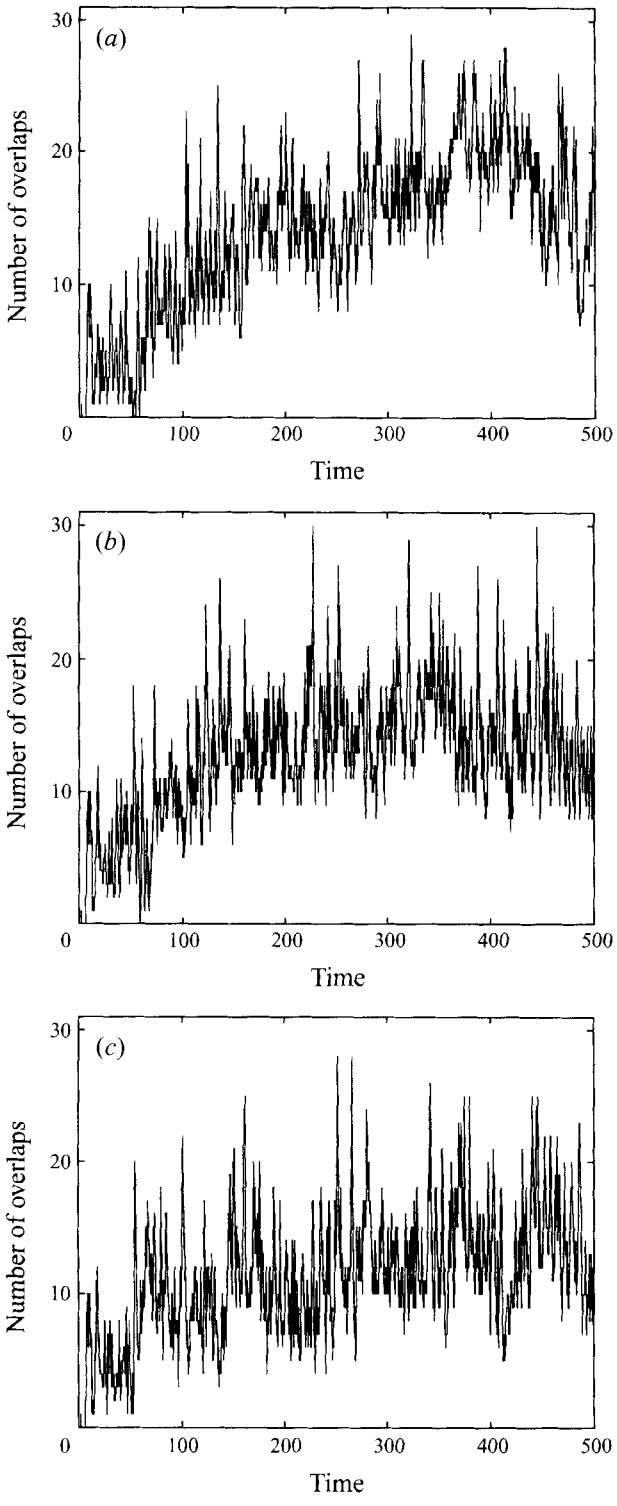

FIGURE 4. The number of particle overlaps in instantaneous particle configurations as a function of time. $\phi_a = 0.50$, $\boldsymbol{F}_p = \mathbf{0}$, $T_s = 500$, $N = 25$. (*a*) $\Delta t = 5.0 \times 10^{-4}$, (*b*) $\Delta t = 2.5 \times 10^{-4}$, (*c*) $\Delta t = 1.25 \times 10^{-4}$.

In addition, computational costs limited $\boldsymbol{F}_p \neq \mathbf{0}$ simulations for which $\phi_a = 0.60$ to $T_s = 250$. For the simulations with $\boldsymbol{F}_p = \mathbf{0}$, $\epsilon = 10^{-8}$ except where noted. The required time step Δt was a function of ϕ_a and τ and ranged from $\Delta t = 10^{-3}$ to 2.5×10^{-5} for simulations of non-repulsive particles, and from $\Delta t = 5 \times 10^{-4}$ to 1.5625×10^{-5} for simulations of repulsive particles. Other numerical parameters employed in the simulations were: $T_{inv} = 0.1$ and $z_{cell} = 100 h_{cell}$. Tests were performed to ensure that results did not change significantly when different numerical parameters or initial configurations were employed.

4.1. *Simulation of non-repulsive particles*: $\boldsymbol{F}_p = \mathbf{0}$

Results presented in this subsection are for non-repulsive particles, i.e. $\boldsymbol{F}_p = \mathbf{0}$. For these types of simulations, particle overlaps occurred for the entire range of areal fractions considered. To illustrate their prevalence, the number of particle overlaps is shown as a function of time for $\phi_a = 0.50$ in figure 4(*a*). Although quite oscillatory, the number of overlaps tends to increase with time, exceeding ten for most of the simulation and exceeding 20 for a significant fraction of time as well. Since 12 overlaps can involve up to 24 particles, 10–20 overlaps in a configuration containing 25 particles is certainly non-trivial.

The simulation discussed above, for which $\Delta t = 5.0 \times 10^{-4}$, was rerun with time steps of $\Delta t = 2.5 \times 10^{-4}$ and 1.25×10^{-4} to determine if the number of overlaps could be reduced by reducing the time step. The number of overlaps as a function of time for these simulations is shown in figures 4(*b*) and 4(*c*). There is only a slight reduction in the number of overlaps, on average, for the simulations employing smaller time steps. This suggests that particle overlaps cannot be eliminated for reasonable values of Δt. Reductions in other parameters that influence the temporal accuracy of the simulations, such as T_{inv}, also had little effect on the number of overlaps. In addition, similar results were obtained using different initial configurations, and for simulations employing 36, 49 and 64 particles. The number of overlaps did increase with increasing N, but remained nearly constant on a per-particle basis. For all values of N, configurations contained on average about one overlap for every two particles. In general, we also found that overlaps became more common with increasing ϕ_a, with usually no more than one overlap per 25-particle configuration at $\phi_a = 0.20$ and up to 40 overlaps per 25-particle configuration at $\phi_a = 0.60$. In addition, for the entire range of areal fractions considered, overlaps could not be eliminated by reducing the time step.

In order to better understand why time-step refinement does not significantly reduce the number of overlaps, it is useful to examine the temporal variation of the surface-to-surface separation h of two nearly touching particles in the $\Delta t = 5.0 \times 10^{-4}$ simulation discussed above. For this purpose, we consider two particles that overlapped in the time interval $6 \leqslant t \leqslant 7$. With the particle configuration at $t = 4$ as an initial condition, the $\Delta t = 5.0 \times 10^{-4}$ simulation was rerun for 3 time units using various values of Δt and ϵ in order to observe the influence of these parameters on h. The time variation of h for these various parameter values, plotted at intervals of Δt, is shown in figure 5 for the time interval $2 \leqslant t \leqslant 3$, which corresponds to the time interval $6 \leqslant t \leqslant 7$ in the original simulation. In the initial configuration, $h = 2.4 \times 10^{-3}$.

The temporal variation of h for $\Delta t = 5 \times 10^{-4}$ and $\epsilon = 10^{-8}$, the same values used in the original simulation, is shown in figure 5(*a*). When h reaches a value of approximately 10^{-8} it decreases rapidly, with the particles overlapping at $t \approx 2.3$. When the particles overlap, $h < 0$ and cannot be plotted on a logarithmic scale and so are omitted from the curves shown in figure 5. The rapid decrease in h seen in figure 5(*a*) is due to the method used to compute hydrodynamic forces that is described in §3.

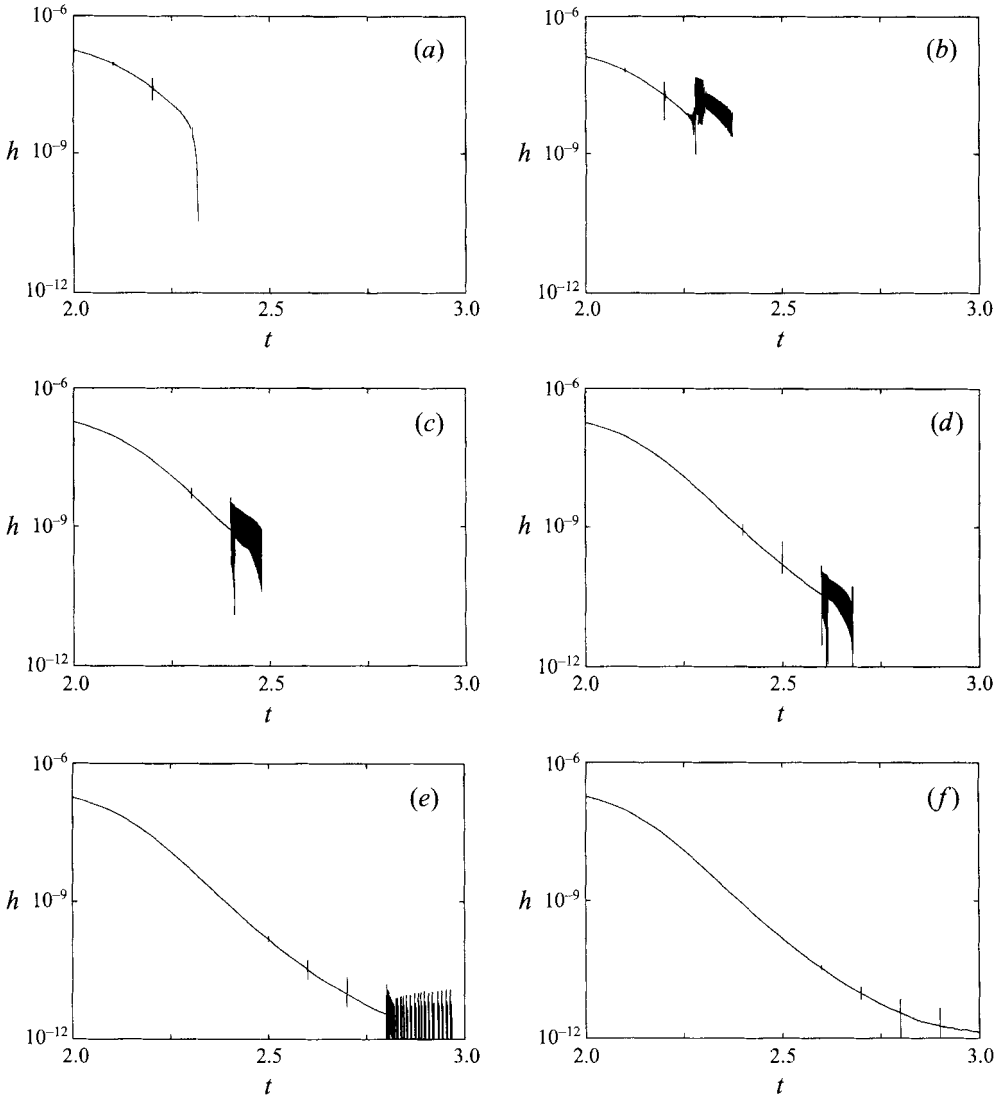

FIGURE 5. Temporal variation of surface-to-surface separation h between two nearly touching particles for various Δt and ϵ. For obvious reasons, negative values of h were omitted from the plots, and h is plotted only up to the point at which significant oscillations or overlaps occur. $\phi_a = 0.50$, $\boldsymbol{F}_p = \boldsymbol{0}$, $N = 25$. (*a*) $\epsilon = 10^{-8}$, $\Delta t = 5.0 \times 10^{-4}$; (*b*) $\epsilon = 10^{-12}$, $\Delta t = 5.0 \times 10^{-4}$; (*c*) $\epsilon = 10^{-12}$, $\Delta t = 1.25 \times 10^{-4}$; (*d*) $\epsilon = 10^{-12}$, $\Delta t = 3.125 \times 10^{-5}$; (*e*) $\epsilon = 10^{-14}$, $\Delta t = 7.8125 \times 10^{-6}$; (*f*) $\epsilon = 10^{-14}$, $\Delta t = 3.90625 \times 10^{-6}$.

Since these forces are computed assuming $h = \max(h, \epsilon)$, lubrication forces are weaker than is physically realistic when $h < \epsilon$ and are insufficient to keep the particles separated. As a result, the particle separation decreases rapidly when $h < \epsilon$, resulting in overlap. The 'kinks' observed in figure 5 are due to the periodic updating of the mobility tensors, which was performed at time intervals of $T_{inv} = 0.1$.

In figure 5(*b*), the time variation of h for $\Delta t = 5 \times 10^{-4}$ and $\epsilon = 10^{-12}$ is shown. For these parameter values, hydrodynamic forces are correctly computed for $h \geqslant 10^{-12}$. This eliminates the rapid decrease in h observed in figure 5(*a*). However, h now becomes oscillatory at $t \approx 2.3$ where $h \approx 7 \times 10^{-9}$. These oscillations cause the particles

to overlap. As observed in figures 5(*c*) and 5(*d*), for which $\Delta t = 1.25 \times 10^{-4}$ and 3.125×10^{-5} respectively, with $\epsilon = 10^{-12}$ for both figures, the onset of the oscillations is delayed by reducing the time step. Additional time-step reductions cause further delays in the onset of the oscillations, as observed in figures 5(*e*) and 5(*f*), for which $\Delta t = 7.8125 \times 10^{-6}$ and 3.90625×10^{-6} respectively, with $\epsilon = 10^{-14}$ for both figures. Although it appears that overlaps have been entirely eliminated for $\Delta t = 3.90625 \times 10^{-6}$, the particles did overlap very briefly at $t \approx 2.9$. In addition, since the particle separation is decreasing with time at $t = 3$, overlaps are likely to occur for $t > 3$. This supports our original contention that overlaps cannot be eliminated for reasonable values of Δt. In all cases for which large oscillations in h occurred, these oscillations led to particle overlap.

We note that the condition number of $\boldsymbol{R}_{FU}$, $\mathrm{con}(\boldsymbol{R}_{FU})$, scales as approximately $1/h_{min}$ where h_{min} is the minimum particle separation in a configuration. For the small values of h shown in figure 5, $\boldsymbol{R}_{FU}$ can be quite ill-conditioned so it is important to determine the effect of this ill-conditioning on computed results. Assuming particle positions, and therefore $\boldsymbol{R}_{FU}$, $\boldsymbol{R}_{FE}$, $\boldsymbol{F}_p$, and $\boldsymbol{U}^\infty$ are accurately known, the error associated with solving equation (5) for $\boldsymbol{U}$ is bounded by $\mathrm{con}(\boldsymbol{R}_{FU}) \| R \| / \| B \|$. Here R is the residual of equation (5), B is the right-hand side of (5), and $\| \ \|$ denotes a vector norm. Therefore, since the position vector $\boldsymbol{X}$ is obtained from time integration of $\boldsymbol{U}$, the error in $\boldsymbol{X}$ directly attributable to error in $\boldsymbol{U}$ is bounded by $\Delta t \, \mathrm{con}(\boldsymbol{R}_{FU}) \| R \| / \| B \|$. For the results shown in figure 5(*f*), $\Delta t = 3.90625 \times 10^{-6}$, the maximum value of $\mathrm{con}(\boldsymbol{R}_{FU})$ is $O(10^{14})$, and $\| R \| / \| B \|$ is assumed to be about 10^{-16} since double-precision (64 bit) arithmetic was used in all of our computations. Therefore the error bound on $\boldsymbol{X}$ is approximately 10^{-8}, which is considerably larger than the smallest value of h in figure 5(*f*).

To determine if the ill-conditioning of $\boldsymbol{R}_{FU}$ adversely influenced the results shown in figure 5, the simulations used to generate the data shown in this figure were rerun using 128-bit arithmetic. With this increased precision, $\| R \| / \| B \| \approx 10^{-32}$ and the error bound on $\boldsymbol{X}$ is about 10^{-24}, which is considerably smaller than the smallest value of h in figure 5. However, results obtained using the increased precision are virtually identical to the results shown in figure 5. Therefore, although $\boldsymbol{R}_{FU}$ is indeed ill-conditioned when h is small, this had no qualitative effect on the results shown in figure 5.

We also note that η can be ill-conditioned when the minimum particle separation in the suspension is small. However, for all of the viscosity results presented in this work, minimum particle separations were 10^{-8} when $\boldsymbol{F}_p = \boldsymbol{0}$ (recall that a minimum separation equal to ϵ is assumed when $\boldsymbol{F}_p = \boldsymbol{0}$) and $O(10^{-5})$ when $\boldsymbol{F}_p \neq \boldsymbol{0}$. For particle separations greater than or equal to these minima, ill-conditioning did not appear to be a problem.

The results shown in figure 5 illustrate two important points. First, the method developed by Bossis & Brady (1984) (see §3) to compute hydrodynamic forces associated with nearly touching and overlapping particles can actually cause overlaps. Secondly, if ϵ is reduced in order to improve the accuracy of the hydrodynamic force computations at small separations, numerical instability becomes a problem due to the stiffness of the evolution equations that describe particle trajectories. This instability also causes particle overlaps. This suggests that numerical instability and associated particle overlaps could be eliminated through the use of an implicit numerical integration scheme. To test this hypothesis, a limited number of simulations were performed using a variable-time-step predictor–corrector algorithm (fourth-order predictor, fifth-order corrector). Although particle overlaps were not observed in these

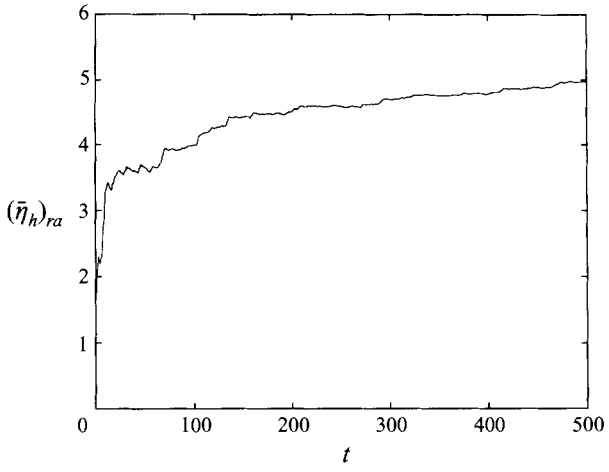

FIGURE 6. Running average of the hydrodynamic component of viscosity $(\bar{\eta}_h)_{ra}$ as a function of time. $\phi_a = 0.50$, $\boldsymbol{F}_p = \mathbf{0}$, $T_s = 500$, $\Delta t = 5.0 \times 10^{-4}$, $N = 25$.

tests, this approach did lead to particle separations smaller than the resolution of double-precision arithmetic (approximately 10^{-16}). Therefore, even if numerical stability problems can be eliminated, one still has the problem of resolving extremely small particle separations. It is important to note that non-continuum effects and physical phenomena not accounted for in the simulations become important at particle separations much larger than those achieved here (e.g. for sphere diameters of 100 μm, a separation of 10^{-8} is equivalent to 5×10^{-13} m). This suggests that non-hydrodynamic forces become important in all suspensions, regardless of particle size, when particles are near contact and need to be included in any realistic model of suspension mechanics. If these forces are omitted, then extremely small particle separations will occur, invalidating the continuum hydrodynamic model and giving rise to related problems such as particle overlaps. In addition, since small particle separations are expected to become more common with increasing density, the consequences of neglecting non-continuum and non-hydrodynamic effects, such as particle overlaps, should also become more common with increasing density. Our results are in agreement with this view and indicate a dramatic increase in the incidence of particle overlaps with increasing density when $\boldsymbol{F}_p = \mathbf{0}$.

A number of simulations were also performed using a variable-time-step explicit Euler integration method. Although particle overlaps were not observed in these simulations, particle separations were quite small, $O(10^{-11})$. Furthermore, these separations decreased with decreasing time step and showed no tendency to converge to non-zero values. This suggests that, in the absence of repulsive interparticle forces, the minimum particle separation will tend to zero with time-step refinement. Therefore, in agreement with results obtained using the predictor–corrector method, we find that even if particle overlaps can be eliminated, one still has the problem of resolving extremely small particle separations. At these small separation distances, non-continuum and non-hydrodynamic forces will undoubtedly be important.

An example of the rheological behaviour of a suspension in which particles are subjected to hydrodynamic forces only, i.e. where $\boldsymbol{F}_p = \mathbf{0}$, is shown in figure 6. In this figure, the temporal dependence of the running average of η_h, denoted here by $(\bar{\eta}_h)_{ra}$, is shown for $\phi_a = 0.50$. These data are from the $\Delta t = 5.0 \times 10^{-4}$ simulation for which particle overlaps are shown in figure 4(*a*). The running average $(\bar{\eta}_h)_{ra}$ displays a strong

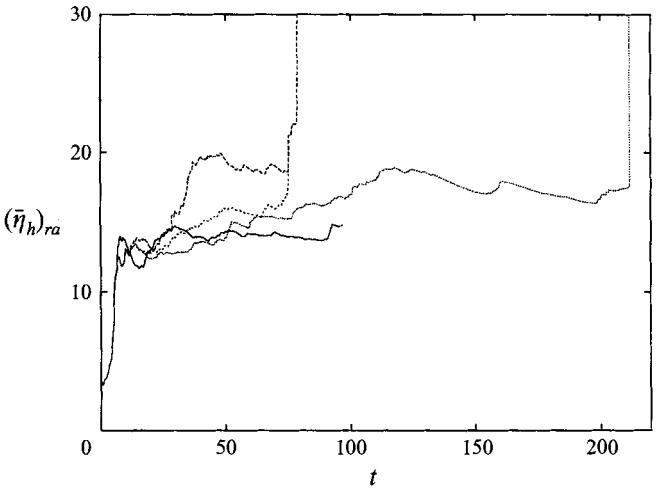

FIGURE 7. Running average of the hydrodynamic component of viscosity $(\bar{\eta}_h)_{ra}$ as a function of time. $\phi_a = 0.60$, $\boldsymbol{F}_p = \boldsymbol{0}$, $N = 25$. ———, $\Delta t = 2.5 \times 10^{-4}$; — — —, $\Delta t = 1.25 \times 10^{-4}$; – – –, $\Delta t = 5.0 \times 10^{-5}$; ···, $\Delta t = 2.5 \times 10^{-5}$.

temporal dependence for $t < 200$, and a weaker but non-trivial temporal dependence for $200 < t < 500$. However, for a suspension whose bulk properties are time-independent, the long-time or asymptotic value of $(\bar{\eta}_h)_{ra}$ should also be time-independent. The continued evolution of $(\bar{\eta}_h)_{ra}$, even after 500 time units, suggests that in the absence of non-hydrodynamic forces, suspensions do not approach an asymptotic state. In contrast to the temporal dependence of $(\bar{\eta}_h)_{ra}$ observed in figure 6, Brady & Bossis (1985) and Chang & Powell (1993) reported equilibration times of 20 for essentially identical simulations.

To further illustrate the rheological behaviour of suspensions simulated using a purely hydrodynamic model, the temporal dependence of $(\bar{\eta}_h)_{ra}$ for $\phi_a = 0.60$ is shown in figure 7. Results are shown for four different time steps: $\Delta t = 2.5 \times 10^{-4}$, 1.25×10^{-4}, 5.0×10^{-5}, and 2.5×10^{-5}. For all four Δt, $(\bar{\eta}_h)_{ra}$ exhibits a strong initial transient that dissipates prior to $t = 10$. Beyond this point, $(\bar{\eta}_h)_{ra}$ appears to plateau. However, for $\Delta t = 2.5 \times 10^{-4}$ the simulation terminated at $t \approx 96$ due to the presence of overlaps in excess of 2% of a particle radius. The more temporally resolved simulations also terminated due to the presence of overlaps in excess of 2%, except for the $\Delta t = 1.25 \times 10^{-4}$ simulation which was run for 500 time units. However, for this case, $(\bar{\eta}_h)_{ra}$ is shown only for $t \lesssim 79$ because the viscosity attained an enormous and likely unphysical value ($\eta_h = O(6000)$) at $t = 78.8$. Interestingly, the more-resolved simulations did not always run longer before terminating (see e.g. the curves corresponding to $\Delta t = 2.5 \times 10^{-4}$ and 5.0×10^{-5} in figure 7). We also note that for all four simulations, the number of overlaps exceeded 40 at the final time point plotted in figure 7. At higher densities termination occurred at smaller times, with simulations for $\phi_a = 0.70$ stopping in less than 40 time units, even with times steps as low as 5.0×10^{-6}. In contrast, this anomalous behaviour was not reported by Chang & Powell (1993), who performed simulations analogous to those discussed here. However, as their $\phi_a = 0.60$ simulations were run for only 40 time units, it is possible they would have observed similar behaviour in longer simulations. These results are additional evidence that Stokesian Dynamics simulations based on a purely hydrodynamic model of particle interactions do not approach an asymptotic state at long times, and therefore do not

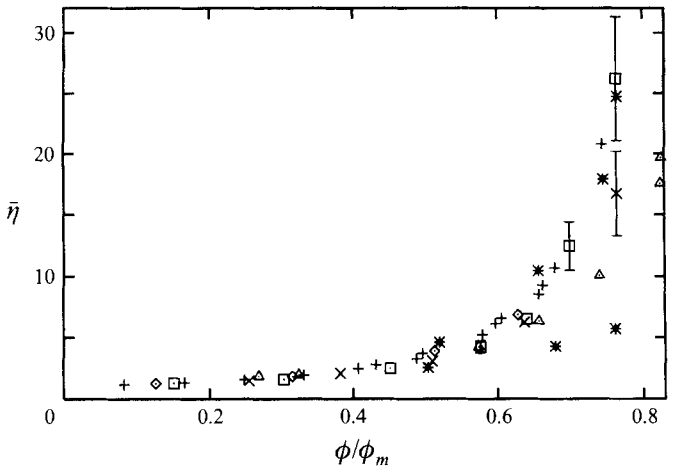

FIGURE 8. Comparison of relative viscosities $\bar{\eta}$ obtained from Stokesian Dynamics simulations ($\times$) to the viscosity data shown in figure 1. For the current work: $\boldsymbol{F}_p = \mathbf{0}$, $N = 25$, and error bars are omitted when smaller than the symbol.

exhibit the behaviour expected of real suspensions. Instead it appears that the suspended particles become more densely packed with time, and that this eventually leads to particle overlaps that grow without bound.

It has been suggested (J. F. Brady 1995, personal communication) that the observed increase in viscosity with time may be a manifestation of a singularity in the pure hydrodynamic limit. To answer this question definitively, in the absence of an analytical proof, one would wish to observe the variation of viscosity with time under conditions such that overlaps were prevented through a sufficiently (perhaps prohibitively) small time step, and the cell size was increased so that $N \rightarrow \infty$. Even if this were computationally possibly, one would not expect the results to mimic real particles since deviations from sphericity and surface forces will surely become important as particle separations approach zero.

Time-averaged viscosities $\bar{\eta}$ for $0.20 \leqslant \phi_a \leqslant 0.60$ are shown in figure 8 where they are compared to the viscosity data shown previously in figure 1. As in figure 1, the data are plotted as a function of ϕ/ϕ_m, with ϕ and ϕ_m as defined previously. We note that the simulation methods used by Brady & Bossis (1985) and Chang & Powell (1993) differ slightly from the method outlined in §2, the main differences being the neglect of hydrodynamic interactions between particles and their images, and the use by Brady & Bossis (1985) of a different method for forming the resistance matrices. Computing time-averaged viscosities from our simulations was somewhat problematic since, as noted above, $(\bar{\eta}_h)_{ra}$, and therefore $(\bar{\eta})_{ra}$, do not become time-independent to the degree expected, particularly at high densities. Therefore, we simply set T_e (the lower bound of the temporal interval used for averaging) high enough so that strong systematic variations in η occurring at short times were excluded from computed averages. However, weaker systematic variations in η occurring at larger times could not always be excluded from computed averages since these systematic variations do not always dissipate prior to the end of the simulation. As a result, computed values of $\bar{\eta}$ are somewhat dependent on T_e, although not to a great degree. In addition, for $\phi_a = 0.60$ the upper bound of the averaging interval was set at 70 time units so as to exclude the unrealistically large values of η that occurred in some simulations.

From figure 8, it is clear that for $\phi_a \leqslant 0.50$ ($\phi/\phi_m \leqslant 0.64$), viscosities from our

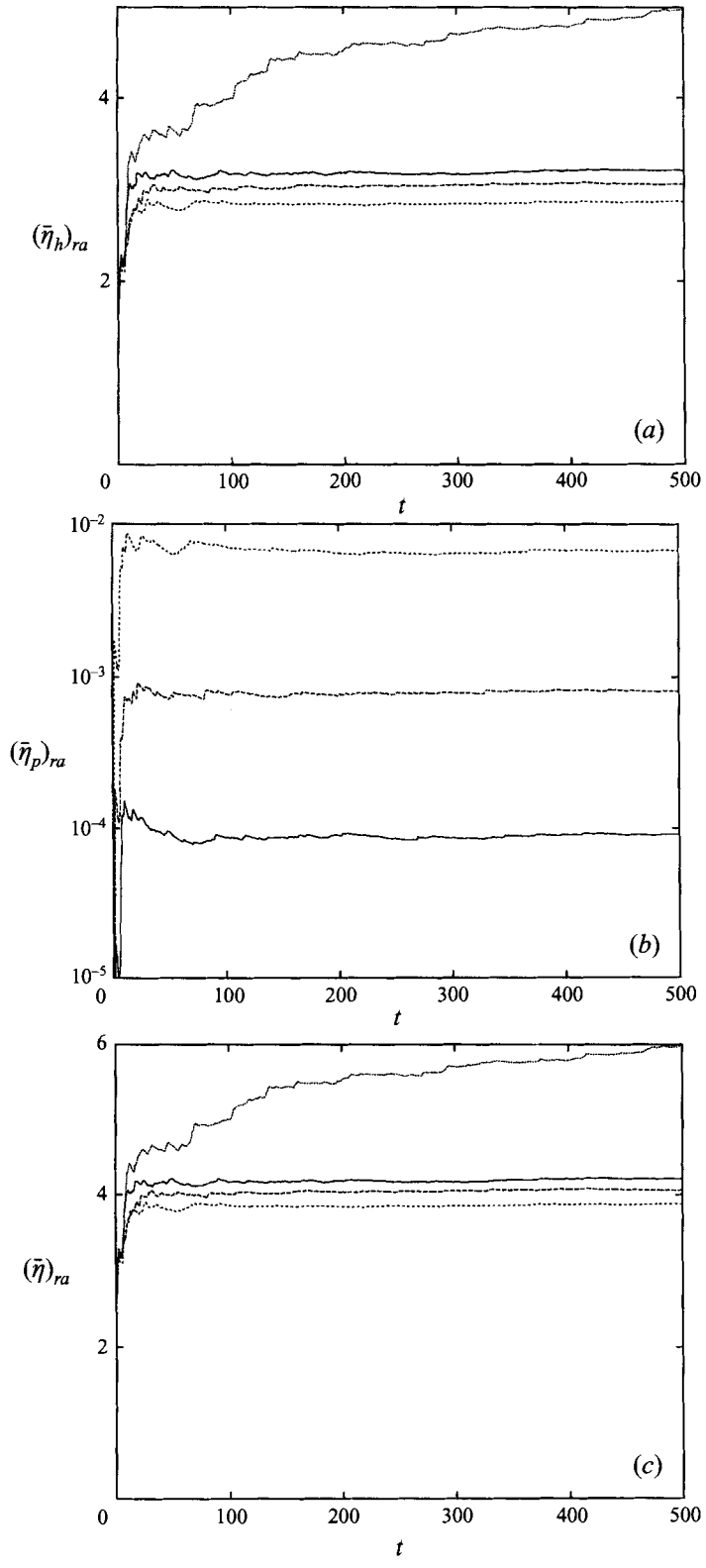

FIGURE 9. Temporal variation of running averages of hydrodynamic, interparticle force, and total viscosities, $(\bar{\eta}_h)_{ra}$, $(\bar{\eta}_p)_{ra}$, and $(\bar{\eta})_{ra}$. $\phi_a = 0.50$, $\gamma^* = 1$, $N = 25$. ———, $\tau = 1.25 \times 10^6$; — — —, $\tau = 1.25 \times 10^5$; – – –, $\tau = 1.25 \times 10^4$; ..., no repulsion. (*a*) $(\bar{\eta}_h)_{ra}$, (*b*) $(\bar{\eta}_p)_{ra}$, (*c*) $(\bar{\eta})_{ra}$.

simulations compare well to the simulated viscosities of Brady & Bossis (1985) and Chang & Powell (1993) and to the experimental data of Lewis & Nielsen (1968), Sengen & Probstein (1989), and Thomas (1965). However, at $\phi_a = 0.60$ ($\phi/\phi_m \approx 0.76$), our computed viscosity, obtained from the $\Delta t = 2.5 \times 10^{-5}$ simulation discussed above, is approximately 40% less than that computed by Chang & Powell (1993) and falls between the two sets of experimental data. For this density, time-averaged viscosities obtained from the simulations discussed in regard to figure 7 ranged from 15 to 21. For the largest of these values, the viscosity of Chang & Powell (1993) is within our 95% confidence interval. As noted previously, overlaps occurred for the entire range of ϕ_a considered. For $\phi_a = 0.60$, up to 40 overlaps per configuration were observed.

4.2. *Simulation of repulsive particles*: $\boldsymbol{F}_p \neq \boldsymbol{0}$

In this subsection we present results of simulations for which the suspended particles are repulsive ($\boldsymbol{F}_p \neq \boldsymbol{0}$), with the repulsion described by equation (9). The parameters τ and γ^*, which control the magnitude and range of $\boldsymbol{F}_p$, were selected so that the range would be small compared to a particle radius (i.e. $\tau \gg 1$) and so that the magnitude would be sufficiently large to prevent overlap. For most of the results shown, $\gamma^* = 1$ and $\tau = 1.25 \times 10^6$.

Allowing the particles to be repulsive has the effect of setting a minimum particle separation in the suspension, thereby eliminating problems associated with extremely small particle separations, such as particle overlap. For $\tau = 1.25 \times 10^6$ and $\gamma^* = 1$, the minimum separation was $O(10^{-5})$ for all areal fractions. For the $O(100\ \mu\text{m})$ particles used in the experiments of Lewis & Nielsen (1968) and Sengen & Probstein (1989), a dimensionless separation of $O(10^{-5})$ corresponds to a dimensional separation of $O(\text{Å})$. Although considerably larger than the minimum separations encountered when $\boldsymbol{F}_p = \boldsymbol{0}$, non-continuum and non-hydrodynamic forces may still be important at these small length scales. In addition, given that deviations from sphericity and surface roughness may be larger than 10^{-5}, in dimensionless terms, particles this close may be considered to be in contact, with $\boldsymbol{F}_p$ representing forces associated with contact.

A criticism of the use of a repulsive force to prevent extremely small particle separations and overlaps is that it destroys the fore-aft symmetry of particle trajectories that exists in the absence of non-hydrodynamic forces. However, the results presented in §4.1, as well as the results of Bossis & Brady (1984), suggest that non-hydrodynamic forces are never truly absent in a real suspension owing to the presence of particles near contact. Therefore, fore-aft symmetry is unlikely to exist in a real system, and need not be replicated in a realistic simulation. We also note that, given the short range of $\boldsymbol{F}_p$, if the particles are well dispersed they will not be influenced by the repulsion and symmetry will be preserved.

For all ϕ_a of interest, simulations were performed for a range of γ^* and τ to ensure that our results did not vary significantly with variations in these parameters. For $\phi_a = 0.30$ and 0.50, simulations were performed for $\gamma^* = 1$ with $\tau = 1.25 \times 10^4$, 1.25×10^5, and 1.25×10^6, and for $\tau = 1.25 \times 10^6$ with $\gamma^* = 0.1$, 1, and 10. For all other areal fractions, simulations were performed for $\gamma^* = 1$ with $\tau = 1.25 \times 10^5$ and 1.25×10^6, and for $\tau = 1.25 \times 10^6$ with $\gamma^* = 1$ and 10. As will be shown for $\phi_a = 0.50$, computed viscosities did not vary significantly with either parameter. For all ϕ_a, $\bar{\eta}$ varied by less than 1% when γ^* was varied and τ was held fixed. For variations of τ with γ^* held fixed, variations in $\bar{\eta}$ ranged from under 1% at $\phi_a = 0.20$ to about 10% at $\phi_a = 0.60$.

Tests were also conducted to ensure that results did not change significantly when

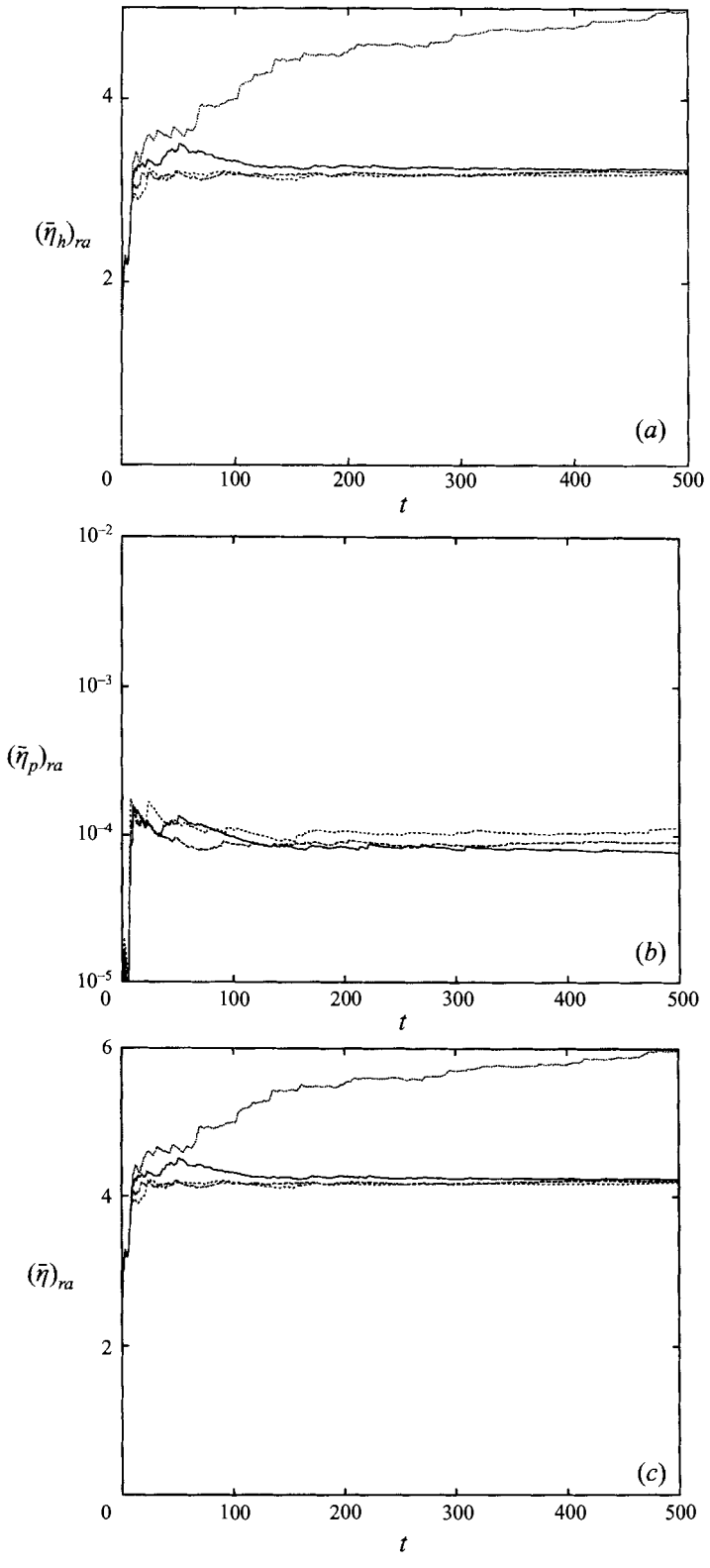

FIGURE 10. Temporal variation of running averages of hydrodynamic, interparticle force, and total viscosities, $(\bar{\eta}_h)_{ra}$, $(\bar{\eta}_p)_{ra}$, and $(\bar{\eta})_{ra}$. $\phi_a = 0.50$, $\tau = 1.25 \times 10^6$, $N = 25$. ———, $\gamma^* = 10$; — — —, $\gamma^* = 1$; – – –, $\gamma^* = 0.1$; ..., no repulsion. (*a*) $(\bar{\eta}_h)_{ra}$, (*b*) $(\bar{\eta}_p)_{ra}$, (*c*) $(\bar{\eta})_{ra}$.

different $\boldsymbol{F}_p$ were employed. For $\phi_a = 0.30$, simulations were performed with $\boldsymbol{F}_p$ given by

$$\boldsymbol{F}_p^{\alpha\beta} = \left(\frac{\sigma}{h}\right)^n \frac{\boldsymbol{r}_{sep}}{|\boldsymbol{r}_{sep}|}, \tag{10}$$

where $\boldsymbol{r}_{sep}$ is defined in §3, $\sigma = 10^{-5}$, and $n = 10$. The values σ and n were chosen so that equation (10) would have a range similar to equation (9) when $\tau = 1.25 \times 10^6$ and $\gamma^* = 1$. For the given values of σ, n, τ, and γ^*, $\bar{\eta}$ obtained from simulations employing equation (10) differed by less than 1 % from $\bar{\eta}$ obtained from simulations employing equation (9).

In addition, tests were conducted to ensure that results did not vary significantly with N or with changes in initial conditions. For $\phi_a = 0.50$, $\bar{\eta}$ varied by less than 2 % when N was increased from 25 to 36, and varied by less than 1 % when a different randomly generated initial configuration was employed.

We also note that $\eta_p \neq 0$, and therefore $\bar{\eta}_p \neq 0$, when $\boldsymbol{F}_p \neq \boldsymbol{0}$. However, for the values of τ and γ^* used in these calculations, $\tau = 1.25 \times 10^6$ and $\gamma^* = 1$, $\bar{\eta}_p/\bar{\eta}$ was quite small and ranged from $O(10^{-7})$ for $\phi_a = 0.20$ to $O(10^{-4})$ for $\phi_a = 0.60$.

For $\phi_a = 0.50$, the sensitivity of computed viscosities to changes in τ and γ^* is illustrated in figures 9 and 10. Running averages of η_h, η_p, and η are shown in figure 9 for $\gamma^* = 1$ and various values of τ. For comparison, $(\bar{\eta}_h)_{ra}$ and $(\bar{\eta})_{ra}$ for $\boldsymbol{F}_p = \boldsymbol{0}$ and $\phi_a = 0.50$ are also shown. For all values of τ, running averages $(\bar{\eta}_h)_{ra}$ (figure 9*a*) vary little beyond $t \approx 50$, indicating the suspension has equilibrated. In addition, the variation of $(\bar{\eta}_h)_{ra}$ with τ is relatively small considering the large variations of τ. At $t = 500$, $(\bar{\eta}_h)_{ra}$ varies by about 12 % when τ changes by two orders of magnitude. In contrast, for $\boldsymbol{F}_p = \boldsymbol{0}$ $(\bar{\eta}_h)_{ra}$ shows a steady upward trend for all $t < 500$, indicating that the suspension has not equilibrated. In addition, in the absence of repulsion $(\bar{\eta}_h)_{ra}$ is significantly larger than for $\boldsymbol{F}_p \neq \boldsymbol{0}$, except at very small times. At $t = 500$, $(\bar{\eta}_h)_{ra}$ for $\boldsymbol{F}_p = \boldsymbol{0}$ is about 55 % larger than the largest value of $(\bar{\eta}_h)_{ra}$ for which $\boldsymbol{F}_p \neq \boldsymbol{0}$. As noted in §4.1, particle overlaps were numerous at $\phi_a = 0.50$ when $\boldsymbol{F}_p = \boldsymbol{0}$.

Running averages of η_p corresponding to the $(\bar{\eta}_h)_{ra}$ shown in figure 9(*a*) are shown in figure 9(*b*). As noted above, η_p is non-zero when $\boldsymbol{F}_p \neq \boldsymbol{0}$. However, $\bar{\eta}_p/\bar{\eta}$ is quite small and ranged from about 2×10^{-5} to about 2×10^{-3} for the given values of τ. For all three values of τ, $(\bar{\eta}_p)_{ra}$ equilibrates at $t \approx 50$. We note that the asymptotic value of $(\bar{\eta}_h)_{ra}$ varies directly with τ while the asymptotic value of $(\bar{\eta}_p)_{ra}$ varies inversely with τ. This dependence is expected since $\boldsymbol{F}_p$ becomes steeper and more short ranged with increases in τ.

Running averages of η are shown in figure 9(*c*). The variation of $(\bar{\eta})_{ra}$ with τ is seen to be quite small, with $(\bar{\eta})_{ra}$ at $t = 500$ varying by less than 10 % over the given range of τ. This is a remarkably small change in viscosity given the large change in τ and indicates that computed viscosities are relatively insensitive to the range of $\boldsymbol{F}_p$. In contrast, these viscosities are significantly lower than the viscosity computed with $\boldsymbol{F}_p = \boldsymbol{0}$. In this figure, $(\bar{\eta})_{ra}$ at $t = 500$ for which $\boldsymbol{F}_p = \boldsymbol{0}$, and for which overlaps are quite numerous, is seen to be about 40 % larger than the largest value of $(\bar{\eta})_{ra}$ for which $\boldsymbol{F}_p \neq \boldsymbol{0}$. This indicates that the impact of overlaps on computed viscosities is quite severe and cannot be ignored at moderate to high densities.

In figure 10, the sensitivity of computed viscosities to changes in γ^* is illustrated. In this figure, $(\bar{\eta}_h)_{ra}$, $(\bar{\eta}_p)_{ra}$, and $(\bar{\eta})_{ra}$ are shown for $\tau = 1.25 \times 10^6$ and $\gamma^* = 0.1$, 1, and 10. The variation of viscosity with γ^* is seen to be quite small, with $(\bar{\eta})_{ra}$ (figure 10*c*) at $t = 500$ varying by about 1 % over the given range of γ^*. In agreement with our

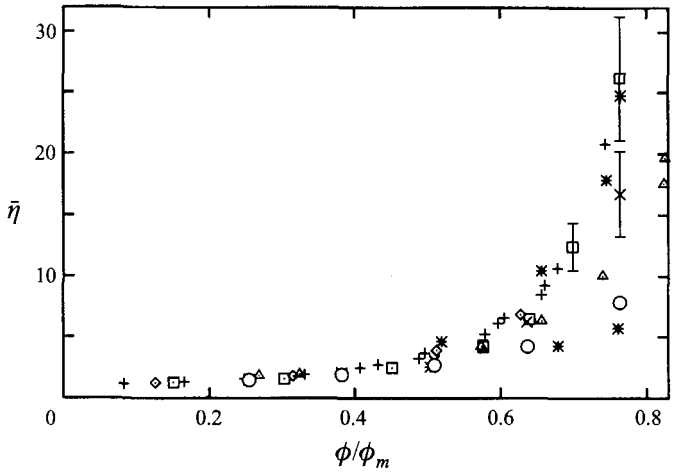

FIGURE 11. Comparisons of relative viscosities $\bar{\eta}$ obtained from Stokesian Dynamics simulations with $\boldsymbol{F}_p \neq \boldsymbol{0}$ (○) to analogous data for which $\boldsymbol{F}_p = \boldsymbol{0}$ (×) from figure 8. Viscosity data from figure 1 are shown for reference. For $\boldsymbol{F}_p \neq \boldsymbol{0}$ data, $N = 25$, $\tau = 1.25 \times 10^6$, $\gamma^* = 1$.

comments at the beginning of this subsection, these results indicate that computed viscosities are relatively insensitive to changes in γ^* and τ.

Time-averaged viscosities $\bar{\eta}$ for $0.20 \leqslant \phi_a \leqslant 0.60$ are shown in figure 11 where they are compared to viscosities obtained from simulations for which $\boldsymbol{F}_p = \boldsymbol{0}$. Simulated viscosities of Brady & Bossis (1985) and Chang & Powell (1993), as well as the experimental measurements of Sengen & Probstein (1989), Lewis & Nielsen (1968), and Thomas (1965) are also shown. For the $\boldsymbol{F}_p \neq \boldsymbol{0}$ results, $\tau = 1.25 \times 10^6$ and $\gamma^* = 1$ for all ϕ_a. For $\phi_a \leqslant 0.40$ ($\phi/\phi_m \leqslant 0.51$), viscosities for which $\boldsymbol{F}_p \neq \boldsymbol{0}$ are in reasonable agreement with those for which $\boldsymbol{F}_p = \boldsymbol{0}$. Agreement with the viscosities of Brady & Bossis (1985) and Chang & Powell (1993) is also reasonably good for $\phi_a \leqslant 0.40$. However, for $\phi_a = 0.50$ and 0.60, viscosities obtained from simulations of repulsive, non-overlapping particles are significantly smaller than for $\boldsymbol{F}_p = \boldsymbol{0}$, and are also significantly smaller than the viscosities of Brady & Bossis (1985) and Chang & Powell (1993). For $\phi_a = 0.60$ ($\phi/\phi_m = 0.76$), the viscosity for which $\boldsymbol{F}_p \neq \boldsymbol{0}$ is 53% smaller than for $\boldsymbol{F}_p = \boldsymbol{0}$ and is 70% smaller than the computed value of Chang & Powell (1993). This suggests that the details of particle interactions when separation distances are small are extremely important at high densities, and significantly impact suspension mechanics and bulk rheological properties.

The viscosities computed with $\boldsymbol{F}_p \neq \boldsymbol{0}$ are seen to compare favourably with the experimental data of Sengen & Probstein (1989), but relatively unfavourably with Lewis & Nielsen (1968). The opposite appears to be true for the data of Brady & Bossis (1985) and Chang & Powell (1993). Viscosities from our simulations with $\boldsymbol{F}_p = \boldsymbol{0}$ fall between the two sets of experimental data. In addition, all four sets of simulated viscosities, and both sets of experimental data, fall within the bounds suggested by the Thomas (1965) data.

However, the presence of extremely small particle separations when $\boldsymbol{F}_p = \boldsymbol{0}$, which calls into question the use of a continuum hydrodynamic model, and the large numbers of overlapping particles that arise from these small separations, are cause for concern and suggest that physics important at small particle separation distances is missing from the pure hydrodynamic model. Therefore, we believe that the pure hydrodynamic model is inadequate for simulating dense suspensions.

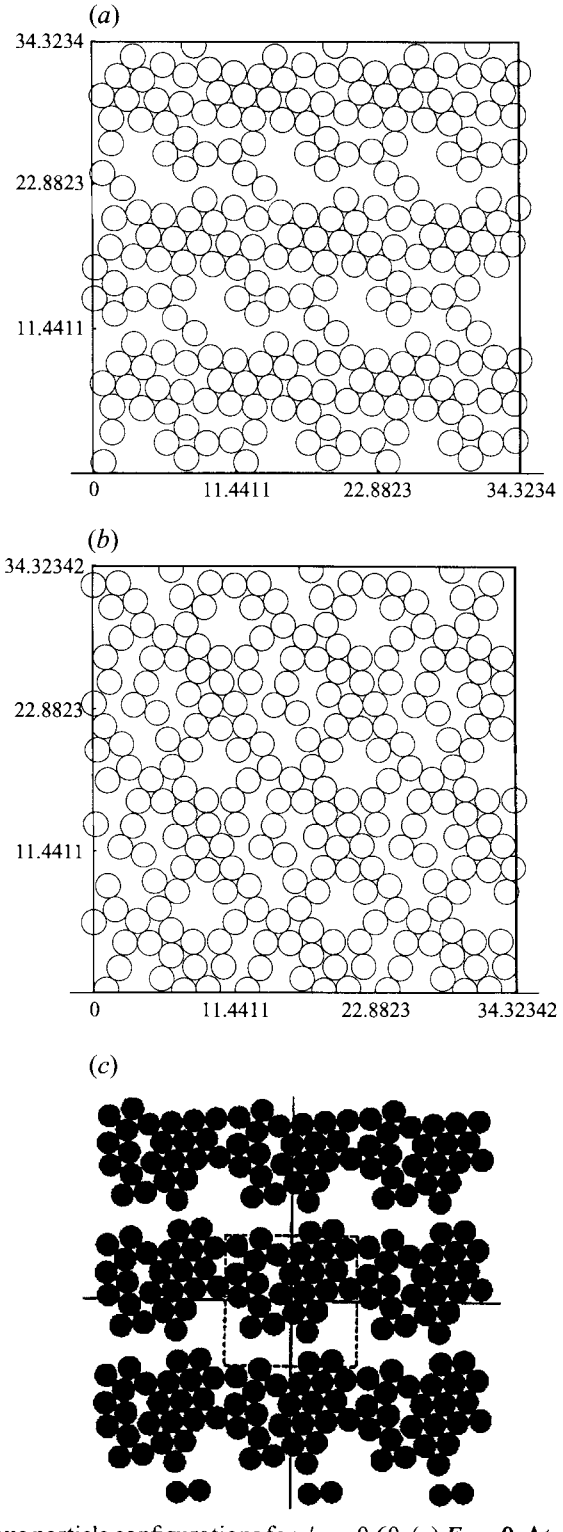

FIGURE 12. Instantaneous particle configurations for $\phi_a = 0.60$. (*a*) $\boldsymbol{F}_p = \boldsymbol{0}$, $\Delta t = 2.5 \times 10^{-5}$, $t = 58.50$; (*b*) $\boldsymbol{F}_p$ given by equation (9) with $\tau = 1.25 \times 10^6$ and $\gamma^* = 1.0$, $t = 189.10$; (*c*) from Chang & Powell (1994). For clarity, and consistency with the data of Chang & Powell (1994), the computational domain has been replicated nine times. $N = 25$.

Additional evidence of the importance of including short-range non-hydrodynamic forces in simulations of non-Brownian hard spheres can be found by examining the suspension microstructure. For $\phi_a = 0.60$, instantaneous particle configurations are shown in figure 12. Figure 12(*a*) shows a configuration for which $\boldsymbol{F}_p = \mathbf{0}$ while figure 12(*b*) shows $\boldsymbol{F}_p \neq \mathbf{0}$ with $\tau = 1.25 \times 10^6$ and $\gamma^* = 1$. For clarity the computational domain in each figure has been replicated nine times. For this same density, an instantaneous configuration from a simulation presented in Chang & Powell (1994) is also shown (figure 12*c*). For the simulation with $\boldsymbol{F}_p = \mathbf{0}$, as well as the simulation of Chang & Powell (1994), all of the particles in the computational domain have aggregated into one large dense cluster that spans the domain in the x-direction. As a result, the particles appear to form layers when multiple computational domains are viewed. In addition, the configuration shown in figure 12(*a*) contains 23 overlaps (not including particle images), which is almost one overlap per particle. In contrast, in figure 12(*b*), particles form clusters that tend to be more linear and tend to align along the compressive axis of the bulk flow. In examining numerous particle configurations from simulations in which $\boldsymbol{F}_p \neq \mathbf{0}$, configurations of the type seen in figure 12(*a*) were never observed.

From examination of the instantaneous configurations shown in figure 12, it is clear that interparticle forces, even those with a very short range, have a significant influence on computed microstructures. However, it is desirable to have a more quantitative measure of microstructural differences than can be obtained graphically. A useful quantity in this regard is $\bar{n}$, the configuration-averaged number of particles that neighbour or abut each particle in the suspension. Here, we consider two particles to be neighbours if their centre-to-centre separation is less than some specified distance r_c. For the simulations used to generate the configurations shown in figures 12(*a*) and 12(*b*), $\bar{n}$ as a function of time is shown in figure 13. For $\boldsymbol{F}_p \neq \mathbf{0}$, $\bar{n}$ is shown for $r_c = 2.01$ and 2.05. For both values of r_c, $\bar{n}$ oscillates about a mean of approximately 2. A value of $\bar{n}$ near 2 is consistent with particle clusters that are linear or string-like, such as those seen in figure 12(*b*). For $\boldsymbol{F}_p = \mathbf{0}$, $\bar{n}$ is shown for $r_c = 2.01$ and 2.00. For $r_c = 2.00$, $\bar{n}$ includes only those particles that touch or overlap other particles in the suspension. For both values of r_c, $\bar{n}$ tends to increase with time and is near 4 at $t \approx 200$. Values of $\bar{n}$ significantly greater than 2 are an indication that particle clusters are two-dimensional. An example of these more two-dimensional clusters is shown in the inset of figure 13, which contains the configuration at $t = 193.80$ from the $\boldsymbol{F}_p = \mathbf{0}$ simulation. For this configuration, for which $\bar{n} = 4.56$, all of the particles have aggregated to form a cluster which is, at least approximately, hexagonally close-packed. In view of the large values of $\bar{n}$ associated with these types of configurations, and the fact that $\bar{n}$ is always near 2 when $\boldsymbol{F}_p \neq \mathbf{0}$, it is clear that clusters of this type do not form when the particles are repulsive.

Finally, we note that $\bar{n}$ depends on the choice of r_c, with $\bar{n}$ an increasing function of r_c and identically zero when r_c is less than the minimum particle separation distance in a configuration. However, for the values of r_c used to generate the data shown in figure 13, significant qualitative variations of $\bar{n}$ with r_c are not observed. This suggests that differences between $\bar{n}$ for $\boldsymbol{F}_p \neq \mathbf{0}$ and $\boldsymbol{F}_p = \mathbf{0}$ are not numerical artifacts, but are indicative of real microstructural differences.

5. Conclusions

Stokesian Dynamics has been used to simulate monolayer suspensions of non-Brownian hard spheres. For the simulations presented in §4.1, particle interactions

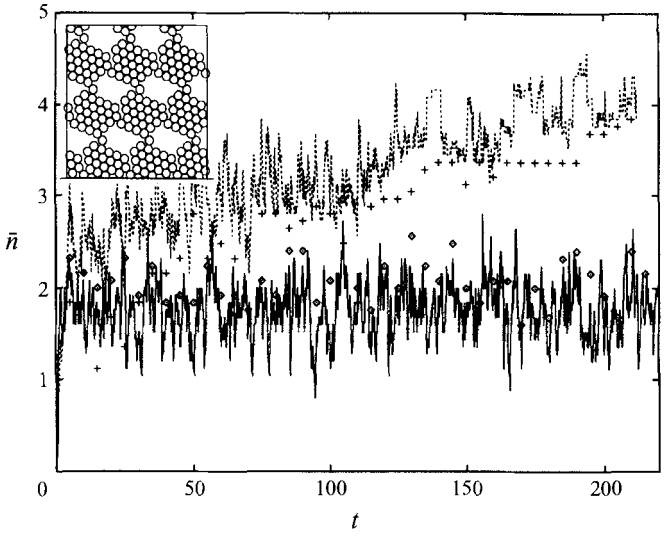

FIGURE 13. $\bar{n}$ as a function of time. $\phi_a = 0.60$, $N = 25$. ———, $\boldsymbol{F}_p \neq \boldsymbol{0}$, $r_c = 2.01$; ◇, $\boldsymbol{F}_p \neq \boldsymbol{0}$, $r_c = 2.05$; – – –, $\boldsymbol{F}_p = \boldsymbol{0}$, $r_c = 2.01$; +, $\boldsymbol{F}_p = \boldsymbol{0}$, $r_c = 2.00$. Inset shows an instantaneous particle configuration at $t = 193.80$ for $\boldsymbol{F}_p = \boldsymbol{0}$, with the computational domain replicated nine times. Data represented by symbols are plotted at five time unit intervals.

were strictly hydrodynamic in nature ($\boldsymbol{F}_p = \boldsymbol{0}$). As a result, distances between particles became sufficiently small to invalidate the continuum hydrodynamic model used for the simulations. Because of the numerical constraints imposed by these small separations, particles tended to overlap. These overlaps became more common with increasing density and could not be eliminated by time-step reductions or by using different numerical methods. At the highest densities considered, the number of overlaps equalled or exceeded the number of particles used in the simulations. In addition, simulations of dense suspensions did not approach asymptotic states at long times, in contradiction to the behaviour of real suspensions. Instead, simulations terminated prematurely due to the presence of large amounts of overlap between adjacent particles. Therefore, despite the fact that simulations based on purely hydrodynamic models of particle interaction have been used to obtain viscosities in reasonable agreement with experimental data, these models lead to physically unrealistic microstructures when one simulates concentrated suspensions.

For the simulations presented in §4.2, particles were subjected to both hydrodynamic and short-range repulsive forces ($\boldsymbol{F}_p \neq \boldsymbol{0}$). This repulsion, which in effect models phenomena important when particles are near contact, completely eliminated extremely small particle separations and associated problems such as overlaps. For all densities considered, the simulated suspensions rapidly approached long-time asymptotic states, with average bulk viscosities showing little variation with run length once the suspensions equilibrated. In addition, disordered microstructures are predicted and computed viscosities are in reasonable agreement with experimental data.

The distinct differences between viscosities for which $\boldsymbol{F}_p = \boldsymbol{0}$ and $\boldsymbol{F}_p \neq \boldsymbol{0}$, which are quite large at high densities, suggest that the dynamics of particles near contact have an important impact on bulk rheological properties and cannot be ignored in realistic models of dense suspensions. Furthermore, our results suggest that critical physics important when particles are near contact is missing from models based solely on continuum hydrodynamics.

Although the focus of this work was non-Brownian suspensions of hard spheres, the issues raised here are likely to be critical whenever particles have a tendency to cluster. For example, in simulations of charge-stabilized suspensions at shear rates above the onset of shear thickening, where microstructures are disordered and contain large clusters of particles, Dratler, Schowalter & Hoffman (1996) were forced to employ the method outlined in §3 to avoid problems associated with small particle separation distances. One is also likely to see clustering, and therefore extremely small separations, in flocculated suspensions and electrorheological suspensions.

Finally, although short-ranged repulsive forces can effectively prevent the problems associated with small particle separations, the computational cost is quite high at high densities. Therefore, more economical methods of dealing with these problems are needed.

The authors wish to thank Professor J. F. Brady for the use of his Stokesian Dynamics simulation code and for important comments on an earlier version of this paper. Financial support for this work has been provided by the Monsanto Company and the University of Illinois. Computations described herein were performed on an IBM RS/6000 workstation provided through the IBM Shared University Research program.

REFERENCES

ALLEN, M. P. & TILDESLEY, D. J. 1987 *Computer Simulation of Liquids*. Clarendon Press.

BATCHELOR, G. K. 1970 The stress system in a suspension of force-free particles. *J. Fluid Mech.* **41**, 545–570.

BONNECAZE, R. T. & BRADY, J. F. 1992 Dynamic simulation of an electrorheological fluid. *J. Chem. Phys.* **96**, 2183–2202.

BOSSIS, G. & BRADY, J. F. 1984 Dynamic simulation of sheared suspensions. I. General method. *J. Chem. Phys.* **80**, 5141–5154.

BOSSIS, G. & BRADY, J. F. 1989 The rheology of Brownian suspensions. *J. Chem Phys.* **91**, 1866–1874.

BRADY, J. F. & BOSSIS, G. 1985 The rheology of concentrated suspensions of spheres in simple shear flow by numerical simulation. *J. Fluid Mech.* **155**, 105–129.

BRADY, J. F. & BOSSIS, G. 1988 Stokesian Dynamics. *Ann. Rev. Fluid Mech.* **20**, 111–157.

BRADY, J. F., PHILLIPS, R. J., LESTER, J. C. & BOSSIS, G. 1988 Dynamic simulation of hydrodynamically interacting suspensions. *J. Fluid Mech.* **195**, 257–280.

CHANG, C. & POWELL, R. L. 1993 Dynamic simulation of bimodal suspensions of hydrodynamically interacting spherical particles. *J. Fluid Mech.* **253**, 1–25.

CHANG, C. & POWELL, R. L. 1994 The rheology of bimodal hard-sphere dispersions. *Phys. Fluids* **6**, 1628–1636.

CONTE, S. D. & BOOR, C. DE 1980 *Elementary Numerical Analysis: An Algorithmic Approach*. McGraw-Hill.

DRATLER, D. I., SCHOWALTER, W. R. & HOFFMAN, R. L. 1996 Dynamic simulation of shear thickening in concentrated colloidal suspensions. *J. Fluid Mech.* (submitted).

DURLOFSKY, L. J. & BRADY, J. F. 1989 Dynamic simulation of bounded suspensions of hydrodynamically interacting particles. *J. Fluid Mech.* **200**, 39–67.

DURLOFSKY, L., BRADY, J. F. & BOSSIS, G. 1987 Dynamic simulation of hydrodynamically interacting particles. *J. Fluid Mech.* **180**, 21–49.

HEYES, D. M. & MELROSE, J. R. 1993 Brownian dynamics simulations of model hard-sphere suspensions. *J. Non-Newtonian Fluid Mech.* **46**, 1–28.

LEWIS, T. B. & NIELSEN, L. E. 1968 Viscosity of dispersed and aggregated suspensions of spheres. *Trans. Soc. Rheol.* **12**, 421–443.

PHUNG, T. & BRADY, J. F. 1991 Microstructured fluids: structure, diffusion and rheology of colloidal dispersions. In *Slow Dynamics of Condensed Matter* (ed. K. Kawasaki, M. Tokuyama & T. Kawakatsu). AIP.

RUSSEL, W. B., SAVILLE, D. A. & SCHOWALTER, W. R. 1989 *Colloidal Dispersions*. Cambridge University Press.

SENGEN, M. Z. & PROBSTEIN, R. F. 1989 High-shear-limit viscosity and the maximum packing fraction in concentrated monomodal suspensions. *PhysicoChem. Hydrodyn.* **11**, 229–241.

THOMAS, D. G. 1965 Transport characteristics of suspension: VIII. A note on the viscosity of Newtonian suspensions of uniform spherical particles. *J. Colloid Sci.* **20**, 267–277.